RSC Advances

PAPER

View Article Online
View Journal | View Issue

Cite this: *RSC Adv.*, 2024, **14**, 4975

An innovative Z-type $Sb_2S_3/In_2S_3/TiO_2$ heterostructure: superior performance in the photocatalytic removal of levofloxacin and mechanistic insight†

Jianrou Li, Zhuangzhuang Yin, Jun Guo, Wei Gan, Ruixin Chen, Miao Zhang* and Zhaoqi Sun*

Received 28th December 2023
Accepted 30th January 2024

DOI: 10.1039/d3ra08905c

rsc.li/rsc-advances

In this study, $Sb_2S_3/In_2S_3/TiO_2$ (SIT) heterojunction photocatalysts were prepared by a simple two-step hydrothermal method and applied to the photocatalytic degradation of levofloxacin (LEV). After 160 min of reaction under visible light, the SIT heterojunction photocatalyst degraded 10 mg L^{-1} LEV at a rate of 86.7%. The degradation of LEV follows pseudo-first-order kinetics with a rate constant 1.16 × 10^{-2} min^{-1}, which is 1.42, 1.22 and 1.05 times higher than that of TiO_2, SI and IT, respectively. Meanwhile, the SIT photocatalysts also showed high photocatalytic activity for other antibiotics. The enhanced photocatalytic activity of the ternary heterostructures was attributed to the full-spectrum response and the synergistic effect of the dual Z-type heterojunctions, which improved the visible light absorption and facilitated the charge separation. In addition, $^{\bullet}OH$ and $^{\bullet}O_2^-$ play a dominant role in the photodegradation process. This work contributes to the design of novel photocatalytic materials with dual Z-type heterojunctions and efficient photocatalysts for the degradation of antibiotics.

1. Introduction

Levofloxacin (LEV) is a third-generation fluoroquinolone antibiotic widely used in human and animal therapy.[1–3] However, due to its complex structure and multiple physicochemical characteristics, it is difficult to completely remove LEV by conventional wastewater treatment techniques, thus it is a serious threat to ecosystems and human health.[4–6] Therefore, it is crucial to explore efficient, direct, eco-friendly and sustainable methods to detect and remove antibiotics from wastewater. Photocatalysis technology based on semiconductor materials has obvious advantages of low cost, environmental friendliness and low-energy, and was considered to be a green chemical pathway with great potential for the treatment of antibiotic wastewater.[7–10] Recently, researchers have studied and developed various photocatalytic materials for the degradation of antibiotics in water. For example, a novel oxygen vacancy-rich $Bi_5O_7Br_xI_{1-x}$ nanorod solid solution was used for the degradation of antibiotic levofloxacin under visible light;[11] construction and actual application of In_2O_3/BiOBr heterojunction for effective removal of ciprofloxacin under visible light;[12] S-scheme heterojunction composite of UiO-66-NH_2/$Bi_7O_9I_3$ was applied for the degradation of ciprofloxacin.[13]

Many semiconductor materials have been designed for photocatalytic degradation of LEVs in wastewater. Among them, titanium dioxide (TiO_2) has low toxicity and good stability, and thus has a wide application potential in water treatment and environmental remediation.[14,15] However, the catalytic performance of pure TiO_2 is affected by the wide band gap (3.2 eV) and high photogenerated carrier recombination rate.[16–18] In order to improve its photocatalytic activity and stability in practical applications, many methods have been proposed, such as optimising the structure of TiO_2 and constructing heterostructures.[19–21]

Since the photocatalytic degradation of antibiotics occurs at the semiconductor–water interface, vertically aligned semiconductor nanoarrays (*e.g.*, nanorods or nanosheets) provide a large number of active sites, reduce carrier diffusion distances and enable multiple light reflections between arrays, which can enhance the photocatalytic degradation of LEVs by improving the photo-generated charge separation efficiency of photocatalyst.[22,23] At the same time, it can also reduce the risk of secondary pollution and improve the environmental friendliness of the wastewater treatment process. More importantly, TiO_2 nanorod arrays provide an exploitable platform for building heterojunction structures. For example, Gan *et al.* used Ag nanoparticles to decorate 2D/2D TiO_2/g-C_3N_4 heterojunction for efficient removal of tetracycline hydrochloride;[24] Guo *et al.* developed a new high-performance ternary photocatalyst based

School of Materials Science and Engineering, Anhui University, Hefei 230601, Anhui Province, P. R. China. E-mail: szq@ahu.edu.cn; zhmiao@ahu.edu.cn

† Electronic supplementary information (ESI) available. See DOI: https://doi.org/10.1039/d3ra08905c

on the co-modification of TiO_2 nanorods with BPQDs and Ag nanoparticles for TC degradation.[25]

Fortunately, the above shortcomings of TiO_2 can be ameliorated effectively by developing a Z-type heterojunction photocatalyst, which can remarkably improve the redox ability of catalysts through enhancing the charge separation efficiency.[26–28] Alternatively, indium sulfide (In_2S_3) has been widely used as a photocatalyst because of its narrow band-gap (2.0–2.3 eV), wide visible light response range and low toxicity.[29–31] On the other hand, antimony trisulfide (Sb_2S_3) has attracted much attention owing to its narrow band-gap (1.5–1.9 eV), large absorption coefficient and so on.[32,33] In_2S_3 and Sb_2S_3 have been chosen to design Z-type composites because of their higher conduct band potential and lower valence band potential.[34,35] According to previous literature, In_2S_3 and Sb_2S_3 have been employed to assemble Z-scheme photocatalysts coupling with other catalysts. Such as, Ding *et al.* prepared In_2S_3/TiO_2 thin-film catalysts with sulfur vacancies for the activated sodium persulfate (PMS) photocatalytic degradation of levofloxacin;[36] Sharma *et al.* fabricated nanoflower-like Sb_2S_3/SiO_2 monoliths by the vacuum impregnation method, which were utilized for the photocatalytic degradation of pollutants MB, TM and real wastewater.[37]

In conclusion, binary Z-scheme photocatalysts have made enough efforts, but their photocatalytic activities still have an improvement room.[38,39] Some studies reported that the successfully synthesized dual Z-type photocatalysts improved the separation/transport efficiency of photogenerated carriers, broadened the photo-response range, and thus enhanced the photocatalytic activity.[40–43] For instance, Jang *et al.* constructed $TiO_2/CdS/MoS_2$ heterojunctions to enhance the photoelectrochemical performance;[44] Shihan Qi *et al.* successfully synthesized In_2S_3/Ag–Ag_2S–$AgInS_2$/TNR photocatalyst by a facile hydrothermal and wet chemical method to enhance the photoelectrochemical and photocatalytic performance;[45] Chen *et al.* constructed $Sb_2S_3/CdS/CdIn_2S_4$ S-scheme heterojunction to improve the photoelectrochemical performance.[46]

In this paper, Z-type $Sb_2S_3/In_2S_3/TiO_2$ (SIT) heterojunction photocatalysts was prepared by a simple two-step hydrothermal method, which was evaluated the performance in the degradation of multiple antibiotics in the visible light and investigated the effect of different experimental parameters on the degradation of levofloxacin (LEV) by SIT. Meanwhile, the main radicals in the photocatalytic system were identified by trapping experiments and electron spin resonance spectroscopy (EPR), and the degradation pathways and intermediates of LEV were revealed by liquid chromatography-mass spectrometry (LC-MS) analysis and three-dimensional excitation-emission matrix fluorescence (3D EEMs). In addition, the energy band structure of the Z-type heterojunction was formulated by the optical and photoelectrochemical properties of the SIT system, and the degradation steps and mechanism of the Z-type SIT photocatalyst were proposed.

2. Experimental

2.1. Material

Fluorine-doped tin oxide (FTO) conducting glasses were obtained from Wuhan Jingge Solar Energy Technology Co., Ltd. Tetrabutyl titanate ($C_{16}H_{36}O_4Ti$, TBT) and thioacetamide (C_2H_5NS, TAA) were obtained from Shanghai Aladdin Biochemical Technology Co., Ltd. Hydrochloric acid (HCl), acetone (C_3H_6O), ethanol, sodium thiosulfate pentahydrate ($Na_2S_2O_3\cdot5H_2O$), and isopropyl alcohol (IPA, $^{\cdot}OH$ scavenger) were obtained from Sinopharm Chemical Reagent Co., Ltd. Ethylene glycol ($C_2H_6O_2$), L-antimony potassium tartrate ($C_8H_4K_2O_{12}Sb_2\cdot xH_2O$), indium(III) chloride tetrahydrate ($InCl_3\cdot4H_2O$), levofloxacin (LEV), and *p*-benzoquinone (BQ, $^{\cdot}O_2^-$ scavenger) were obtained from Macklin Industries Co. Ltd. Ethylenediaminetetraacetic acid disodium (EDTA–2Na, h^+ scavenger) were obtained from Beijing Innochem Science & Technology Co., Ltd. 5,5-Dimethyl-1-pyrroline-*N*-oxide (DMPO) was purchased from Dojindo Chemical Co., Ltd. All chemicals were used as received without further purification.

2.2. Preparation of TiO_2 nanorods arrays

Synthesis of TiO_2 nanorods arrays was made by hydrothermal method. Typically, 0.5 mL of $Ti(C_4H_9O)_4$ precursor was added to 30 mL aqueous solution of 6 M HCl to form a uniform system under stirring. The solution was then transferred to a polytetrafluoroethylene (PTFE) reactor liner (50 mL) and FTO of 2 cm × 5 cm was immersed in the solution. Heating at 150 °C for 12 h. After cooling, the precipitate was washed with deionized (DI) water and ethanol. And dried at 60 °C in an oven overnight.

2.3. Preparation of $Sb_2S_3/In_2S_3/TiO_2$

The fabrication procedure of $Sb_2S_3/In_2S_3/TiO_2$ is illustrated in Scheme 1. 30 mg of TAA and 6 mg of $InCl_3\cdot4H_2O$ were dissolved

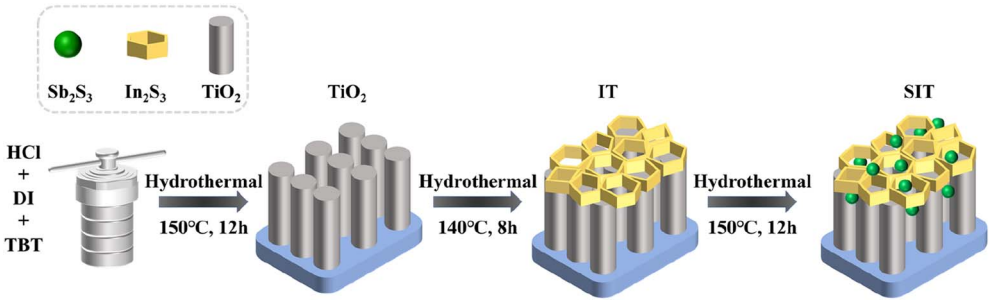

Scheme 1 Synthesis route of SIT.

in 40 mL of ethylene glycol solution. After stirring for 30 min, 10 mg of $C_8H_4K_2O_{12}Sb_2 \cdot xH_2O$ was added to it and stirred for another 30 min, and the prepared TiO_2 nanoarrays were immersed in the solution and heated at 140 °C for 12 h to obtain $Sb_2S_3/In_2S_3/TiO_2$, defined as SIT. In the absence of $InCl_3 \cdot 4H_2O$, single-phase In_2S_3/TiO_2 can also be prepared in a similar method and denoted as IT, Sb_2S_3/In_2S_3 was fabricated by a similar procedure in the absence of TiO_2, defined as ESI.†

2.4. Characterization

The X-ray diffraction (XRD, D8 Advance, Bruker) analyses was performed with a scanning range from 10° to 80° to identify the crystal structures of the samples. The surface morphology of the samples was revealed by field-emission scanning electron microscopy (FESEM, Hitachi S-4800). The microstructure and lattice spacing were analyzed by transmission electron microscopy (JEOL, JEM-F200), which attached energy-dispersive X-ray (EDX) spectroscopy. X-ray photoelectron spectroscopy (XPS; ESCALAB-250) was selected to explore the surface chemical compositions with an Al Kα source. Using the Thermo Avantage software fit the data and the 284.8 eV C 1s internal standard peak as the calibration point. The ultraviolet photoelectron spectroscopy (UPS) data were equipped with He I (21.22 eV) as the UV excitation source. The time-resolved photoluminescence (TRPL) spectra of the samples were obtained by ultrafast time-resolved fluorescence spectrometer (FluoroMax-4P) with an excitation wavelength of 375 nm. The electron paramagnetic resonance (EPR) spectra were performed using an electron paramagnetic resonance spectrometer (Bruker EMX Plus). The intermediates produced during the degradation of LEV were determined by liquid chromatography-tandem mass spectrometry (LC-MS).

The analytical methods were provided in ESI.†

2.5. Optical and photoelectrochemical measurements

A fluorescence spectrophotometer (FL, Hitachi F-4500) at a wavelength of 325 nm was used to analyze the separation efficiency of electron–hole pairs. And three-dimensional excitation–emission matrix fluorescence spectrum (3D EEMs) was measured to monitor the fluorescence change during the process of LEV degradation. UV-vis diffuse reflectance spectra (UV-vis DRS) was acquired using a UV-visible spectrophotometer (Shimadzu, UV-2550) and transformed into absorption spectra.

A three-electrode electrochemical workstation (CHI660D) was used to performed the photocurrent response and electrochemical impedance spectroscopy (EIS). 0.1 M Na_2SO_4 solution as electrolyte, sample as working electrode, platinum wire as counter electrode and saturated Ag/AgCl electrode as reference electrode.

2.6. Photocatalytic tests

The photocatalytic performances of all samples were irradiated under a 300 W Xe lamp (Perfect light, PLS-SXE300/300UV). All

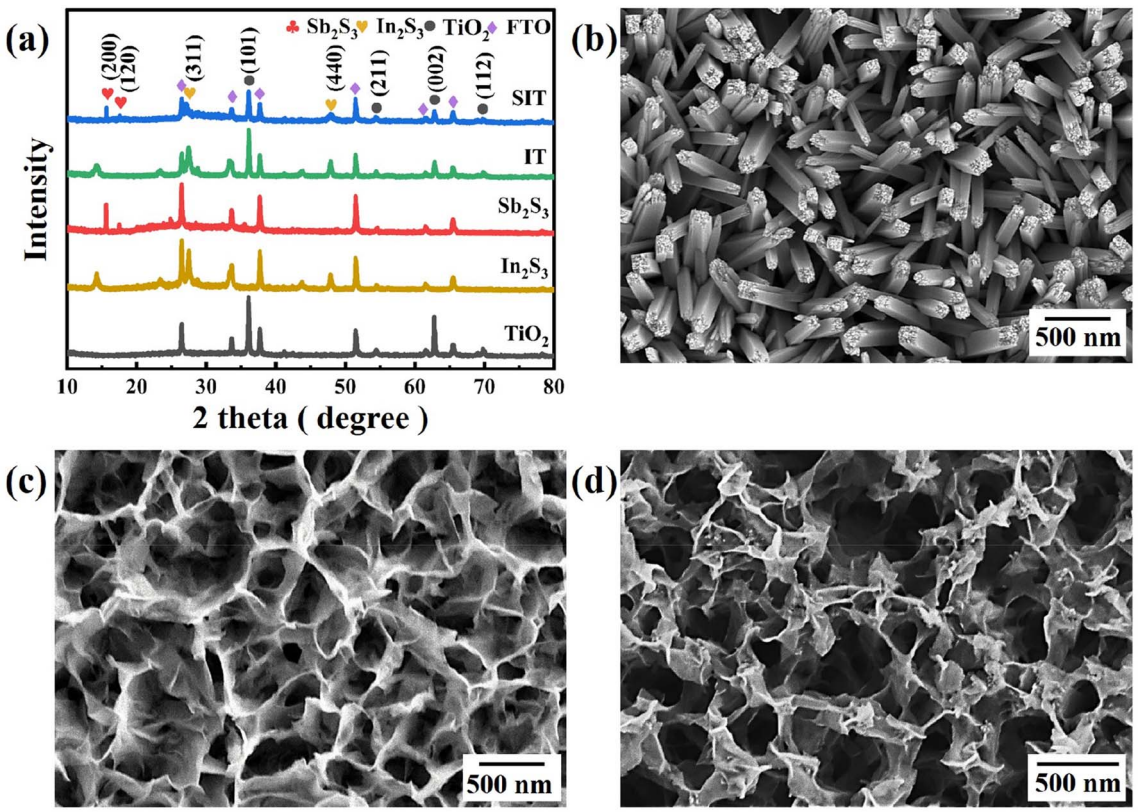

Fig. 1 (a) XRD patterns of pure TiO_2, In_2S_3, Sb_2S_3, IT and SIT; SEM images of (b) TiO_2, (c) IT, (d) SIT.

samples (1 cm × 1 cm) were placed into LEV solution (5 mL, 10 mg L^{-1}) for 30 min under dark condition to achieve the adsorption–desorption balance. The distance between the sample and the light source was set to 10 cm. The intensity of the characteristic absorption peak of the LEV solution was measured by UV-vis spectrophotometer every 30 min. The initial pH for assessing LEV-catalyzed degradation was adjusted with 0.10 M HCl and 0.10 M NaOH.

Additional information is available in the ESI.†

3. Results and discussion

3.1. Structure and morphology characterization

X-ray diffraction (XRD) pattern of SIT is depicted in Fig. 1(a). Neglecting the diffraction peaks of FTO, the characteristic peaks at 36.1°, 54.3°, 62.8° and 69.8° can be identified as the (1 0 1), (2 1 1), (0 0 2) and (1 1 2) planes of rutile TiO_2 (JCPDS 21-1276), respectively. And the peaks at 27.5°, 33.4° and 43.8° belong to (3 1 1) and (4 4 0) planes of In_2S_3 (JCPDS 32-0456), respectively. Moreover, the peak at 15.7° and 17.5° are ascribed to (2 0 0) and (1 2 0) planes of Sb_2S_3 (JCPDS 42-1393). TiO_2 and IT were also synthesized as control samples as shown in Fig. S1(a) and (b).† The main diffraction peaks of SIT coincide with the planes of TiO_2, In_2S_3, and Sb_2S_3, respectively.

The SEM image shows the vertically aligned TiO_2 nanorods are uniformly distributed on the FTO surface with an average width of 120 nm (Fig. 1(b)) and a length of about 1 μm (Fig. S2(a)†). To better disclose the interface effect of SIT heterostructure nanoarrays, those single-phased In_2S_3 and Sb_2S_3 were also prepared. As revealed in Fig. S2(b) and (c),† the In_2S_3 shows the wrinkled nanosheet structure and the Sb_2S_3 displays the particle structure. In Fig. 1(c), the obtained IT composites possess similar morphology to pristine In_2S_3. After anchoring the nanoparticles of Sb_2S_3, the SEM image of SIT in Fig. 1(d) also clearly presents wrinkled structure nanoarrays that were assembled by small nanosheets, as revealed by the SEM image of In_2S_3 and IT. The cross-section view of SIT displays still vertically aligned nanorods arrays in Fig. S2(d).†

As depicted in Fig. 2(a), TEM image of SIT can be clearly seen that the Sb_2S_3 nanoparticles and In_2S_3 nanosheets are successfully anchored on the TiO_2 nanorods, confirms the intimate contact of the In_2S_3 and Sb_2S_3 with TiO_2 nanorods. The highresolution transmission electron microscope image (HRTEM) in Fig. 2(b) suggests three types of clear lattice fringes of 0.32 nm, 0.20 nm and 0.35 nm are respectively attributed to the (1 1 0) plane of TiO_2, the (5 1 1) plane of In_2S_3 and the (1 3 0) plane of Sb_2S_3. In addition, high-angle annular dark-field scanning TEM (HAADF-STEM) image and energy-dispersive X-ray spectroscopy (EDS) mapping images in Fig. 2(c)–(h) observe that all the Ti, In, Sb, O, and S elements were distributed on the whole nanoarrays, which also verifies the above characterizations. Above observations suggest the successful fabrication of heterostructured SIT nanoarray.

XPS analysis was also employed to investigate the chemical state and elemental composition of as-synthesized samples.[47] As shown in Fig. 3(a), the XPS survey spectrum of SIT confirm the existence of expected Ti, In, Sb, S, and O elements, which is consistent with the elemental mapping analysis. Seen from the Ti 2p spectrum of Fig. 3(b), two characteristic peaks of Ti^{4+} state in TiO_2 could be determined as Ti $2p_{3/2}$ at 458.6 eV and Ti $2p_{1/2}$

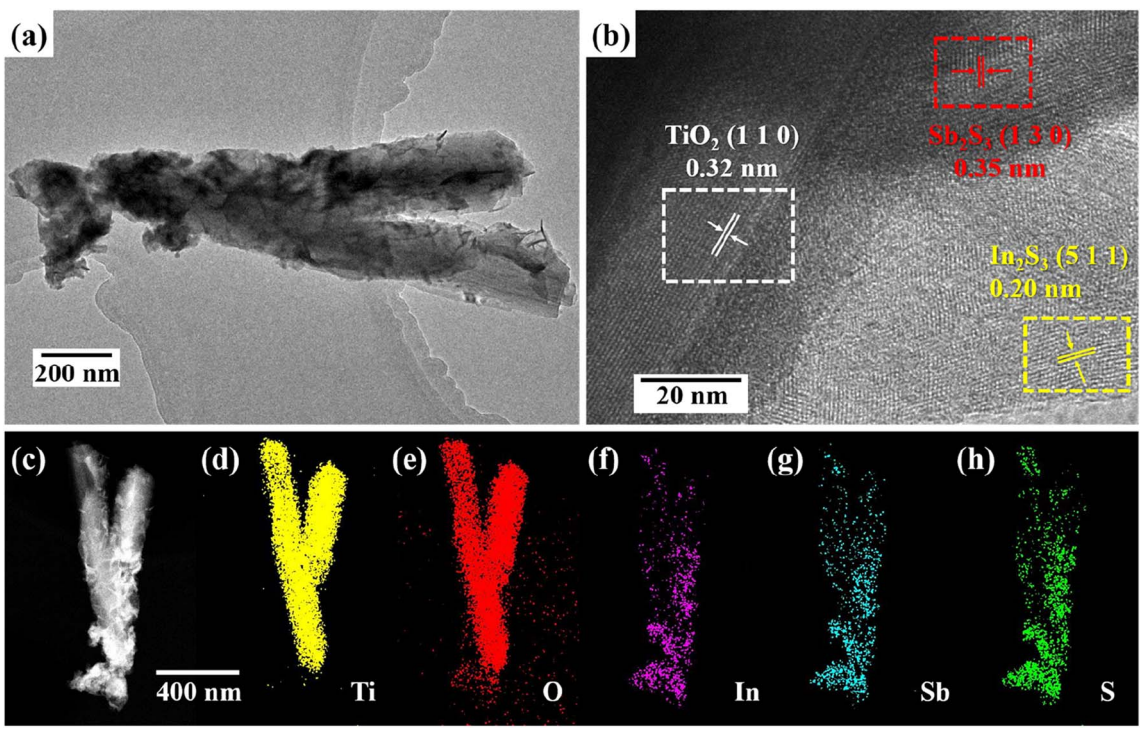

Fig. 2 TEM images of the SIT (a); HRTEM images of a representative region (b); HAADF-STEM image (c); EDS mapping results of SIT (d)–(h).

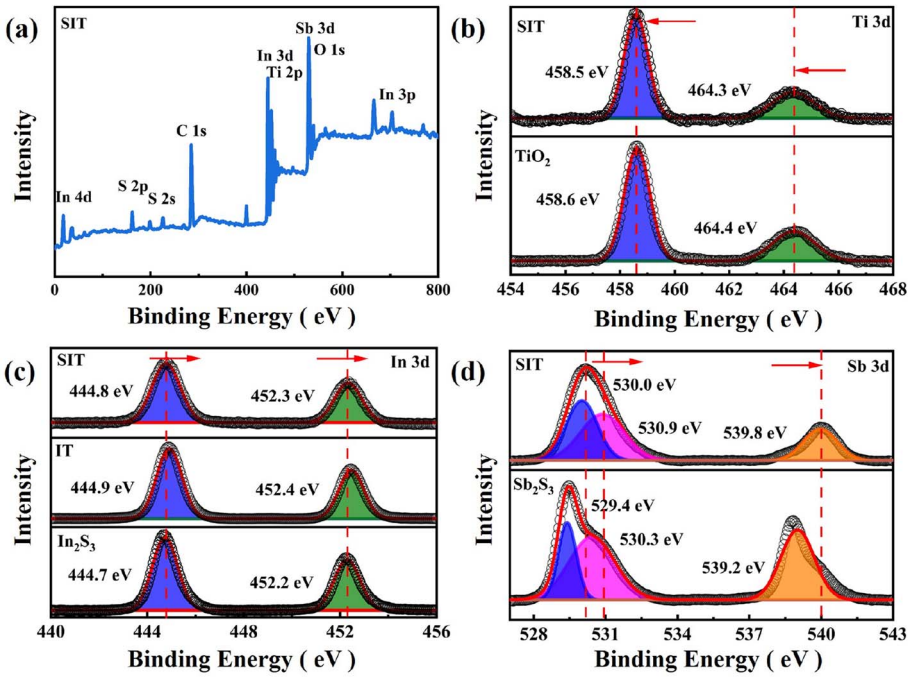

Fig. 3 XPS spectra of different samples: (a) survey spectra, (b–d) the high-resolution spectra of Ti 2p, In 3d and Sb 3d.

at 464.4 eV. After manufacturing SIT, the Ti $2p_{3/2}$ and Ti $2p_{1/2}$ peaks exhibit a negative shift to the binding energies of 458.5 eV and 464.3 eV. As for O 1s spectra in Fig. S3(a),† deconvoluted O 1s peak consists of 531.1 and 530.1 eV, ascribed to the ˙OH group of surface adsorbed H_2O and Ti–O bond in the structure of TiO_2, respectively.[24,48] Similarly, the peaks for O 1s of SIT also indicate slight negative shift.

The In 3d spectrum in Fig. 3(c) reveals that two peaks of In_2S_3 are fitted into $2p_{1/2}$ at 452.2 eV and $2p_{3/2}$ at 444.7 eV. Compared with In_2S_3, the characteristic peaks of SIT are positively shifted by 0.1 eV. Fig. 3(d) presents the Sb 3d spectrum, the peaks of Sb_2S_3 at 529.4 and 539.2 eV are assigned to Sb $3d_{5/2}$ and Sb $3d_{3/2}$ of Sb^{3+}. Similarly, the Sb 3d spectrum of SIT also displays a shift toward the higher binding energy direction. In addition, the peak at 530.9 eV could be attributed to the oxidation of the catalyst surface in the air.[32,46] The S 2p spectrum in Fig. S3(b)† is segmented into the peaks at 161.3 and 162.5 eV, attributed to S $2p_{1/2}$ and S $2p_{3/2}$ of SIT, respectively.

Furthermore, the binding energy of an element is closely related to its density of outer electrons.[27,40] The abovementioned analysis confirms that the binding energies of TiO_2 move towards a high energy region, while the binding energies of In_2S_3 and Sb_2S_3 offset to a low energy region, which implies a low electron density of TiO_2 and a high electron density of In_2S_3 and Sb_2S_3 in the heterostructure of SIT. The phenomenon demonstrates that the electrons migrate from TiO_2 to In_2S_3 and Sb_2S_3 in the Z-type heterojunction of SIT.

3.2. Photocatalytic activity

3.2.1. Performance of different systems for LEV degradation. LEV degradation under visible light was used to assess the photocatalytic activity of each produced photocatalyst. The experimental parameters were pH = 7, photocatalyst size of 1 cm × 1 cm and initial LEV concentration of 10 mg L^{-1}. To achieve the equilibrium between absorption and desorption, all photocatalytic devices were left in the dark for 30 min. The solutions were then exposed to a Xe radiation for 160 min. In order to increase the validity of the trials and confirm the stability of LEV under lighting conditions, blank experiments were also carried out. In Fig. S4(a),† the UV-visible spectra of the photocatalytic degradation of LEV by the SIT system. The distinctive peak of LEV at 288 nm gradually shrinks, as LEV continues to break down and produce a huge number of intermediates. LEV molecules broke down into tiny molecules after 160 min.

For all produced photocatalysts, the removal rate (η) and kinetic constants (K_a) of LEV photodegradation were determined using eqn (S1) and (S2),† and the results are shown in Fig. 4(a) and (b) and S4(b).†[25,36] The η of TiO_2 degradation of LEV was about 61.2% with a K_a of 5.94×10^{-3} min^{-1}, which could be attributed to its broad forbidden band and low visible light reactivity of the photocatalyst. When compared to the pure TiO_2 photocatalyst, the composites of IT and SI demonstrated superior photocatalytic performance (η = 82.7%, $K_a = 9.59 \times 10^{-3}$ min^{-1} and η = 70.9%, $K_a = 8.23 \times 10^{-3}$ min^{-1}). In particular, when the SIT double Z-type heterojunction composite was utilized as a photocatalyst (Fig. S4(b)†), 86.7% of the LEV was degraded ($K_a = 1.16 \times 10^{-2}$ min^{-1}), which was 1.42, 1.22 and 1.05 times higher than that of TiO_2 SI and IT, respectively. These facts imply that the synergistic effect produced by building a dual Z-type heterojunction delivers the maximum photocatalytic activity of SIT composites, which can be employed as an easily recyclable photocatalyst for efficient LEV degradation. Thus, the following explanations for the greater catalytic activity of SIT:

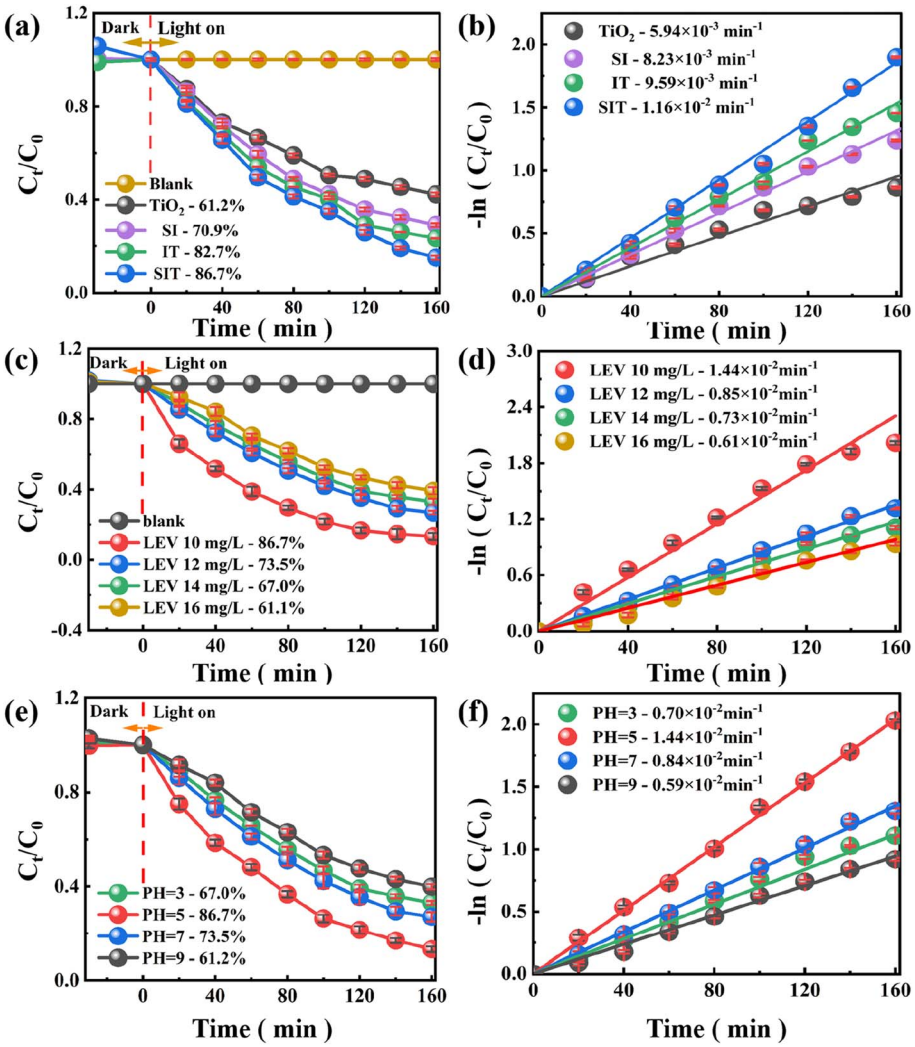

Fig. 4 Effects of reaction parameters on the degradation of LEV (a) different systems, (b) the apparent constant of different catalysts, (c) LEV concentration; (d) the apparent constant of different LEV concentration, (e) initial pH and (f) the apparent constant at different initial pH (reaction conditions: [LEV] = 10 mg L^{-1}; [photocatalyst size] = 1 cm × 1 cm; pH = 7; T = 25 °C; [reaction time] = 160 min for LEV removal).

(1) The TiO_2 vertical nanorod array is distinct in that it has a large specific surface area and more ion transport channels than other structure, which can expose an increasing number of active sites and make them more favorable for reactant adsorption.[22,45]

(2) The dual Z-type heterostructure, which fosters contact and a synergistic effect among the three materials, achieves successful charge separation and transfer. Additionally, the production of many reactive radicals speeds up the photocatalytic degradation of SIT system.[38,43]

(3) With the addition of Sb_2S_3 component, the visible light absorption range of the composites increased and the light absorption ability of SIT was improved.[32,37]

3.2.2. Effect of LEV concentration. The photocatalytic activity is significantly influenced by the initial concentration of the pollutant. Degradation tests were performed at concentrations of 10, 12, 14, and 16 mg L^{-1} to examine the impact of initial LEV concentration on Xe lamp photodegradation activity. As seen in Fig. 4(c), (d) and S4(c),† the photocatalytic degradation rate dropped from 86.7% to 61.1% and the K_a value decreased from 1.44 × 10^{-2} min^{-1} to 0.61 × 10^{-2} min^{-1} when the initial concentration of LEV was increased from 10 mg L^{-1} to 16 mg L^{-1} while the quantity of SIT remained constant (Fig. S4(c)†). This can be explained by the comparatively small number of radicals produced in the greater concentration of LEV solution, together with the fact that the intermediates produced were adsorbed on the surface of SIT, which left LEV occupying a relatively limited number of catalytically active sites.[2,7] To get the greatest photocatalytic activity, an LEV concentration of 10 mg L^{-1} was used throughout the tests.

3.2.3. Effect of initial pH. Since the pH of the solution affects the ionization state of the target pollutant molecules and the surface electrical characteristics of the catalyst, which in turn affects the degradation reaction, therefore pH plays a significant role in photocatalytic degradation.[17,23] The investigation into the impact of pH in the range of 3.0 to 9.0 on the LEV photodegradation efficiency of SIT is depicted in Fig. 4(e), (f) and S4(d).† LEV degraded most effectively overall at pH = 7,

where it degraded by roughly 86.7%. The removal efficiency of LEV in the acidic medium region declined with decreasing pH; the photodegradation of LEV by SIT also shown poor efficiency in extremely alkaline conditions. According to the literature, LEV molecules are cationic (protonated piperazine groups) at pH $\leq$ 6.02, amphoteric at 8.15 > pH > 6.02, and anionic (deprotonated carboxyl groups) at pH $\geq$ 8.15. The photodegradation effectiveness of LEV decreases because both LEV and SIT are positively charged at media pH = 3 or 5 and negatively charged at media pH = 9, thus creating an electrostatic repulsion that prevents LEV molecules from adhering to the catalyst surface.[27,44] Some of the negative/positive LEV adsorbed on the negative SIT at pH = 7, which increased the effectiveness of LEV photodegradation. As a result, the ideal pH value was found to be 7.

3.3. Universality, reusability and stability

As shown in Fig. 5(a), (b) and S4(e),† the prevalence and usefulness of SIT heterojunctions were determined by the degradation efficiency of various antibiotics, including ampicillin (AMP), gatifloxacin (GAT), chlortetracycline hydrochloride (CHI) and levofloxacin (LEV) to assess their applicability. Surprisingly, under the same experimental conditions, SIT heterojunctions showed good degradation of CHI and LEV with removal efficiencies of 86.7% and 81.2%, respectively, and K_a values of 1.44 $\times$ 10^{-2} min^{-1} and 1.18 $\times$ 10^{-2} min^{-1}, while it showed weaker degradation of GAT and AMP with degradation efficiencies of 67.0% and 28.8%, and K_a values of 0.73 $\times$ 10^{-2} min^{-1} and 0.27 $\times$ 10^{-2} min^{-1}. The intrinsic molecular structure of the antibiotic may be responsible for the significant difference in K_a values. These results confirm that SIT dual Z-type heterojunctions show wide applicability in degrading various antibiotics.

The reusability and stability of the catalysts were investigated to assess their potential for practical applications. As seen in Fig. 5(c), even though the LEV removal efficiency showed a slight decreasing trend as the cycle number increased, the degradation rate of LEV by the SIT dual Z-type heterojunction photocatalyst could still reach 81.7% after four consecutive cycles, indicating that the system has a relatively beneficial cycling performance. Since oxygen-containing functional groups are the primary active ingredient in the degradation of LEV by the SIT system, it can be assumed that the decreased degradation rate of the SIT dual Z-type heterojunction photocatalyst was likely caused by the deactivation of oxygen-containing functional groups as a result of repeated vacuum drying, leaching of metal ions, or adsorption of intermediates.[20,39]

Furthermore, Fig. 5(d) shows the XRD diffractograms of fresh and used catalysts, indicating that SIT maintains its initial crystal structure after repeated use with no significant changes in diffraction peaks. Thus, it has efficient and stable catalytic performance for LEV degradation.

3.4. Identification of reactive oxygen species

As shown in Fig. 6(a) radical trapping experiments were performed to investigate the mainly oxidizing species of SIT

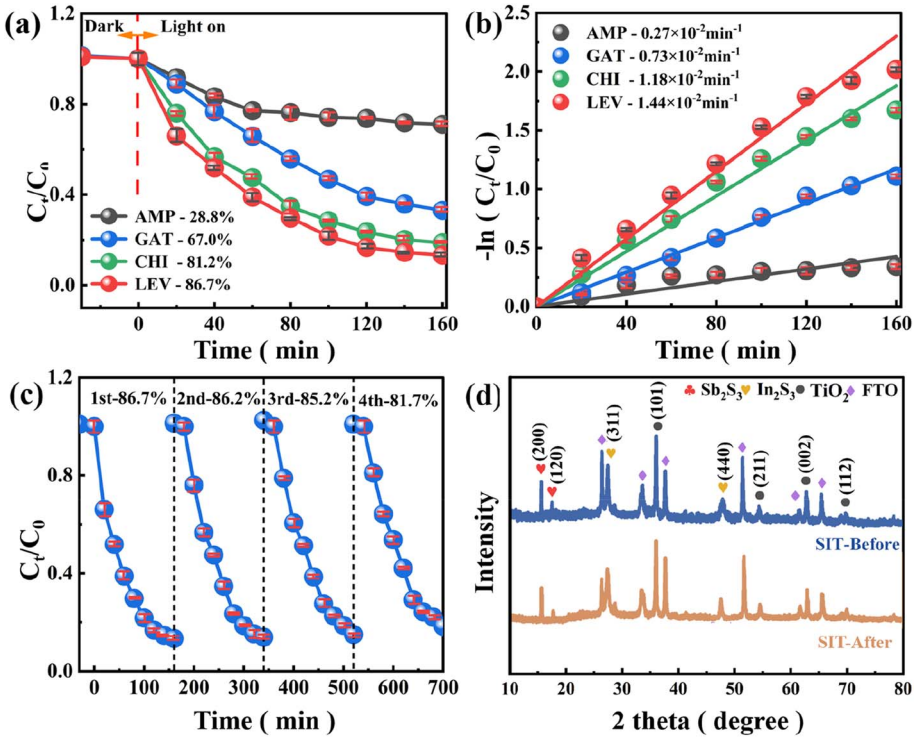

Fig. 5 (a) Universality test, (b) the apparent constant of different antibiotics, (c) reusability test (reaction conditions: [AMP] = 10 mg L^{-1}, [GAT] = 10 mg L^{-1}, [CHI] = 10 mg L^{-1}, [LEV] = 10 mg L^{-1}; [photocatalyst size] = 1 cm × 1 cm; pH = 7; T = 25 °C; [reaction time] = 160 min) and (d) the XRD patterns of SIT before and after the recycling process.

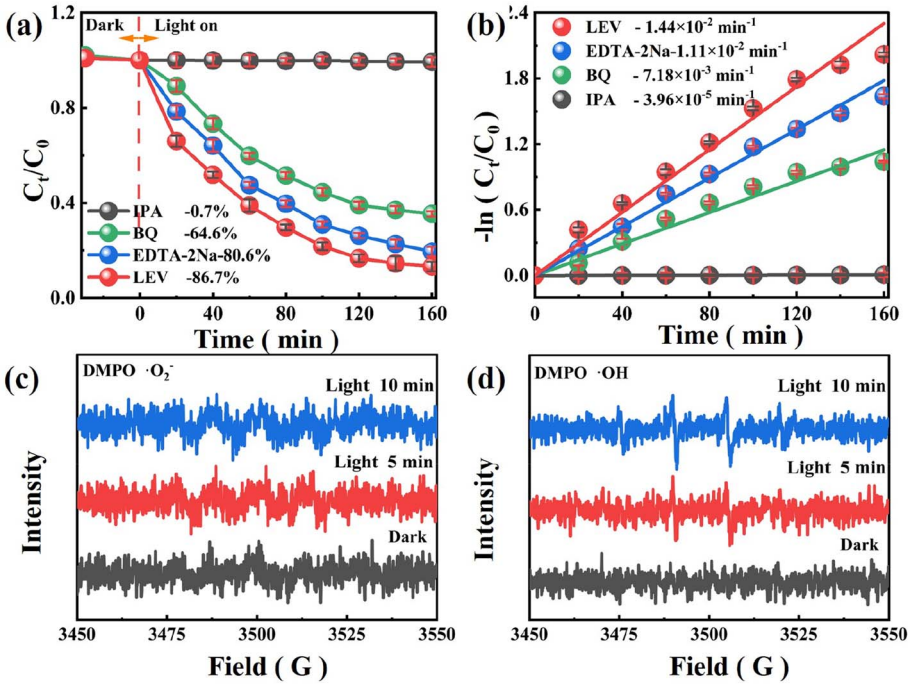

Fig. 6 (a) LEV degradation efficiency and (b) reaction kinetics with various scavengers; the EPR spectra of (c) $^{\bullet}O_2^-$ and (d) $^{\bullet}OH$.

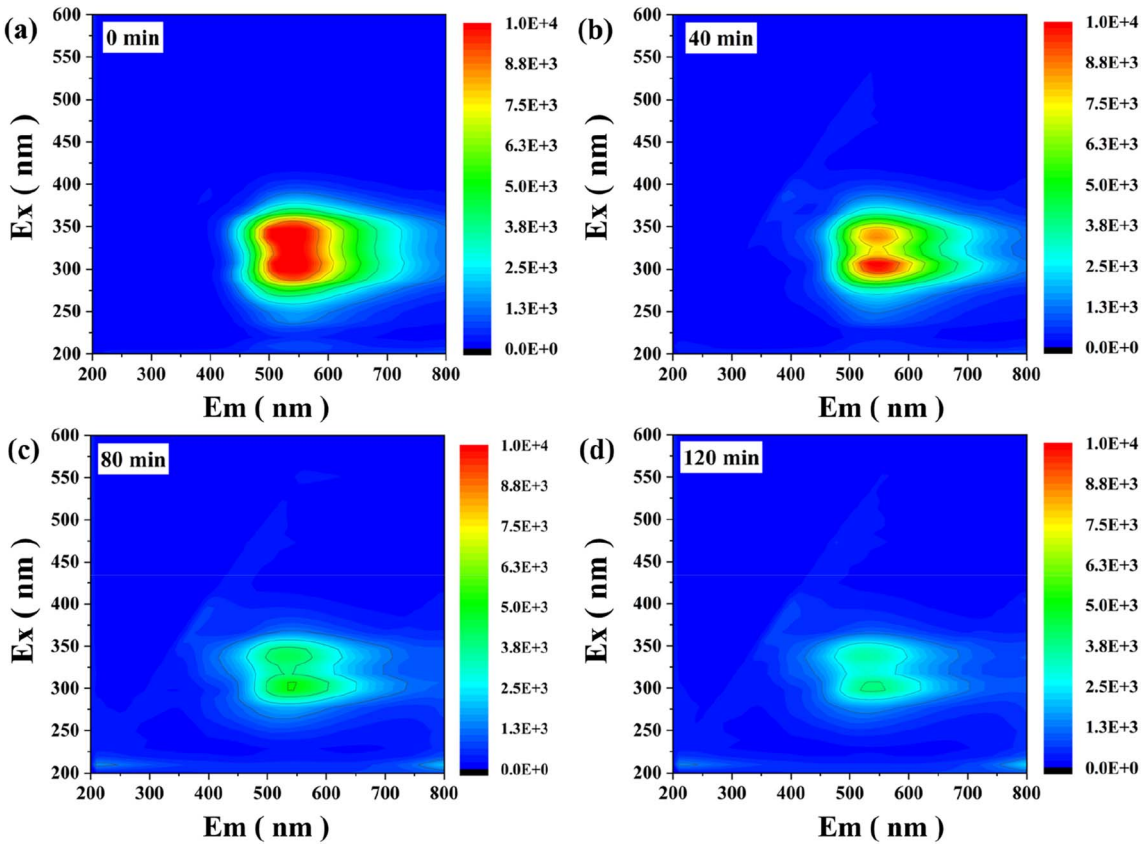

Fig. 7 3D EEMs of the LEV solution after degradation of (a) 0, (b) 40, (c) 80 min and (d) 120 min by SIT. (reaction conditions: [LEV] = 10 mg L^{-1}; [catalyst] = 0.2 cm^2 mL^{-1}; pH = 7; T = 25 °C; [reaction time] = 160 min).

involved in photocatalytic degradation of LEV. Basically, isopropyl alcohol (IPA), *p*-benzoquinone (BQ) and disodium ethylenediaminetetraacetate (EDTA–2Na) were used as the capture agents of hydroxyl radicals ($^{\bullet}OH$), holes (h^+), superoxide radicals ($^{\bullet}O_2^-$) and holes (h^+), respectively.[49] In Fig. 6(b) and S4(f),† the removal rate of LVF decreased dramatically from 86.7% to 0.7% after the addition of 5 mM IPA ($k = 3.96 \times 10^{-5}$ min^{-1}), indicating the presence and dominance of $^{\bullet}OH$ radicals. With the present of 5 mM EDTA–2Na, the degradation efficiency of LEV decreased a little to 80.6% ($k = 1.11 \times 10^{-2}$ min^{-1}), revealing that h^+ was contributed little to the degradation of LEV. Subsequently, BQ at 5 mM resulted in a reduction of LEV removal to 64.6% ($k = 7.18 \times 10^{-3}$ min^{-1}), indicating that $^{\bullet}O_2^-$ was present in the system but was not the dominant radical.

EPR tests were conducted to further confirm the existence of $^{\bullet}O_2^-$ and OH active species with DMPO as the spin trap, the existence of visible light was the only difference.[28,40] EPR spectrum tests in the dark reveal no obvious signal. Fig. 6(c) appeared a 1 : 2 : 2 : 1 signal of DMPO–$^{\bullet}OH$, when the $^{\bullet}OH$ was captured by DMPO, which further confirmed the presence of $^{\bullet}OH$. Similarly, the four signals of 1 : 1 : 1 : 1 were detected in Fig. 6(d), but the peak of DMPO–$^{\bullet}O_2^-$ intensity was weak, which indicated that a few $^{\bullet}O_2^-$ can be generated.[29,35] Above all, $^{\bullet}OH$ and $^{\bullet}O_2^-$ are recognized the domain reactive species in this system.

3.5. Proposed degradation pathways

The obtained 3D EEMs spectra provide important information on the fluorescence changes during LEV degradation.[21,50] Here, Ex represents the emission wavelength (nm) and Em represents the excitation wavelength (nm). As shown in Fig. 7(a), two obvious humus acid-like peaks located at Ex/Em = (320–360/450–600) nm and Ex/Em = (270–320/400–450) nm. The intensity of fluorescence peaks obviously decreased when extending the reaction time to 40 min, implying that the conjugated heterocycle structure of LEV was destroyed (Fig. 7(b)). Moreover, the intensity of the fluorescence peaks continued to decrease with the increase of illumination time (Fig. 7(c)). After 120 min of light illumination (Fig. 7(d)), there is almost no obvious fluorescence signal, exhibiting that the intermediate products of LEV are decomposed into small molecules and eventually mineralized to H_2O and CO_2.

The intermediates and potential degradation pathways of LEV degradation by SIT were identified by LC-MS.[4,47] The obtained mass spectra and intermediates were depicted in Fig. S5–S6 and Table S1,† respectively. Based on previous similar reports, four possible degradation pathways of LEV were proposed, as shown in Fig. 8. In pathway I, the product P1 (m/z = 391) was formed by carboxylation. Then, the intermediates passed through decarboxylation to degrade to P2 (m/z = 374).[44] After the oxazine ring being destroyed, the production of P3 (m/z = 245) from P2 was attributed to the defluorination and

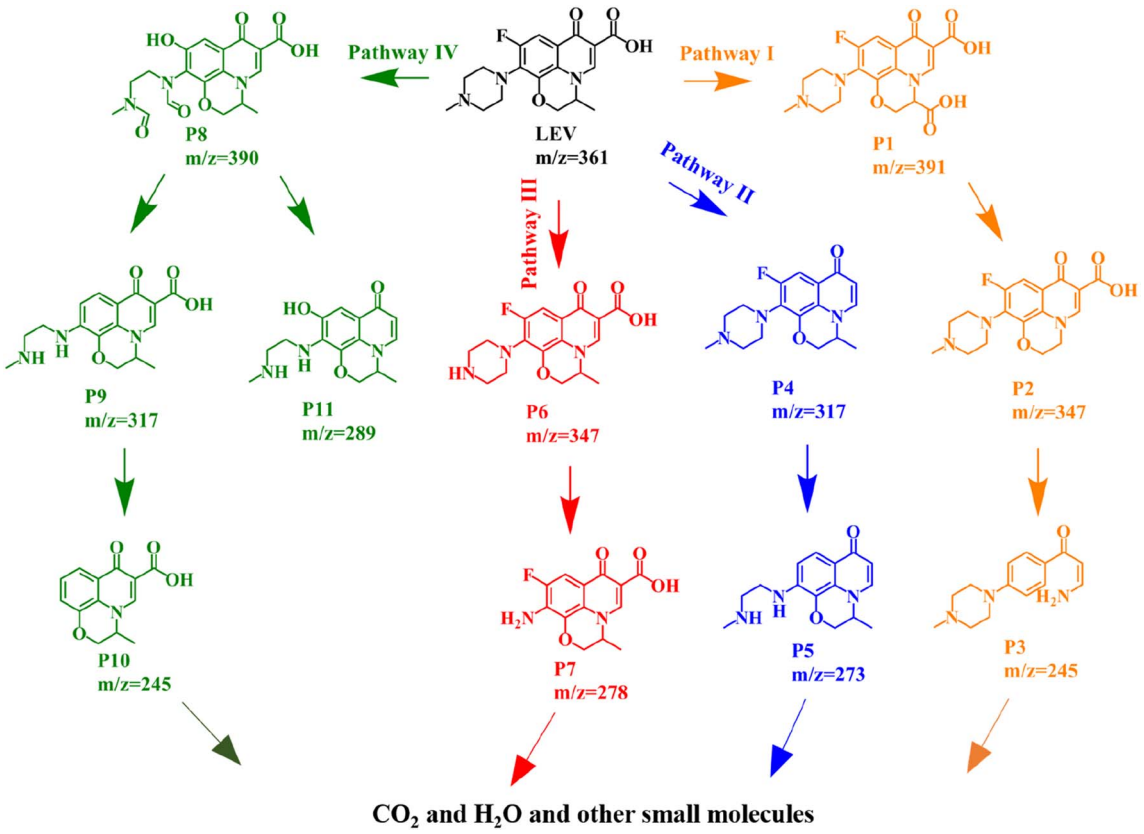

Fig. 8 The proposed degradation pathways for LEV in the SIT system.

decarboxylation.[3] As for pathway II, LEV undergoes decarboxylation to form the P4 ($m/z = 317$).[27] P4 was further reduced and removed by fluorination to produce P5 ($m/z = 273$).[40] Further, take off the piperazine ring to obtain P7 ($m/z = 278$).[46] Pathway IV, P8 ($m/z = 390$) was produced by changing fluorine group into hydroxyl group while opening and oxidizing piperazine ring.[4] Next, P9 ($m/z = 317$) was generated by the cleavage of the hydroxyl group and demethylation to obtain product P10 ($m/z = 245$).[20] Simultaneous, the production of P11 ($m/z = 289$) from P8 were attributed to the removal of C=O bond and decarboxylation.[51] Finally, the intermediates might be further generated to CO_2, H_2O and other small molecules.

Meanwhile, Fig. S7(a)† presents the changes of total organic carbon (TOC) during the degradation process of LEV. After 160 min of light irradiation, TOC removal rate of LEV by the SIT reaches 68.5%. The result further indicates that the structure of LEV is indeed broken and decomposed into H_2O and CO_2 as well as some intermediate products during the process of photocatalytic degradation. Thus, it shows that SIT has good degradability as well as mineralization ability towards LEV.

3.6. Optics and photoelectrochemical investigations

Relevant research shows that the higher the PL intensity, the higher the electron–hole recombination rate and the weaker the photocatalytic performance.[6] PL spectra of TiO_2, IT and SIT were shown in Fig. 9(a), the samples exhibited a strong emission peak centered at 467 nm, the PL intensity of SIT as comparison to TiO_2 and IT was weaker, which indicates that it has high efficiency of photogenerated electron–hole separation.[45] In addition, the charge separation kinetics of the samples were investigated *via* time-resolved photoluminescence (TRPL) spectroscopy. In Fig. 9(b), the lifetime (τ) of TiO_2, IT and SIT were 0.23 ps, 0.20 ps and 0.12 ps, respectively. This result confirms that SIT had the shortest electron lifetime, suggesting the fastest charge transfer of electrons across electrode/electrolyte interface in SIT photoanode.[24] The ability of photogenerated carriers to separate and migrate can be easily observed in the photocurrent density curve.[19] Fig. 9(c) exhibits the transient photocurrent under visible light with light on–off cycles, the photocurrent response density of SIT (52.3 A cm^{-2}) showed the higher current density than that of IT (39.7 μA cm^{-2}), SI (30.1 μA cm^{-2}) and TiO_2 (19.7 μA cm^{-2}). When the lamp was turned off, the current quickly decreased to the initial value. As reported, the radius of semicircle arc represents the charge transfer resistance.[45] As shown in Fig. 9(d), the EIS spectra display that the arc radius of SIT was smallest than those of IT, SI and TiO_2, indicating the lowest electrical impedance and the highest carrier transfer efficiency.[25]

3.7. Photocatalytic mechanism

The UV-vis DRS absorption spectrum of the prepared material was used to investigate the photo-absorption was shown in

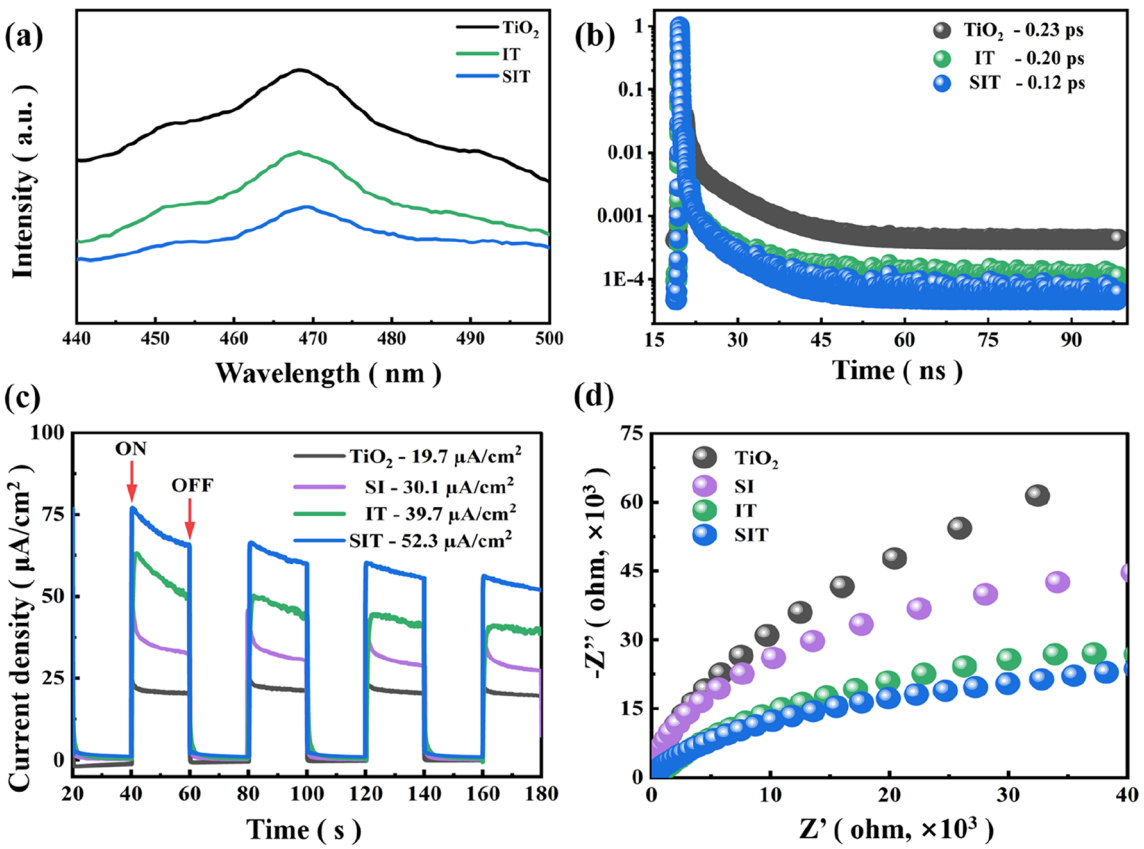

Fig. 9 (a) PL (under the 405 nm laser light excitation) and (b) time resolved PL lifetime plots of TiO_2, IT and SIT; (c) transient photocurrent response and (d) EIS impedance plots of TiO_2, IT, SI and SIT.

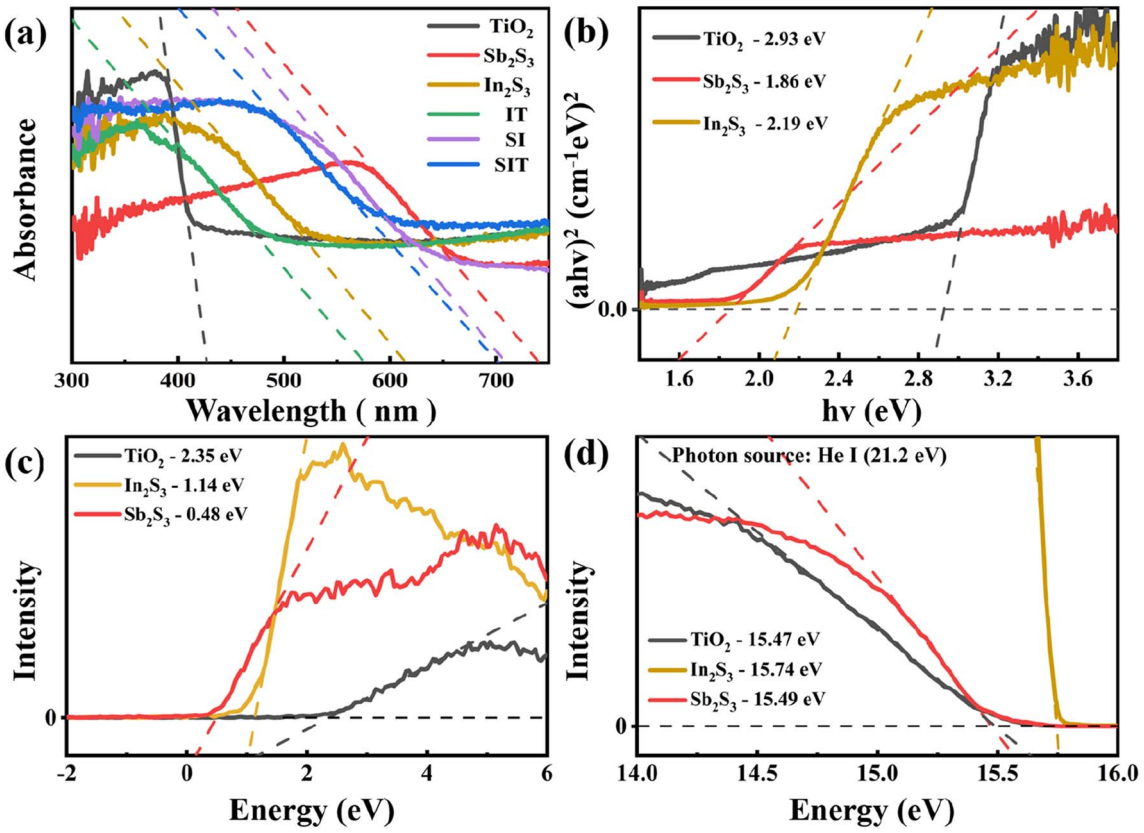

Fig. 10 (a) UV-vis absorption spectra of TiO_2, In_2S_3, Sb_2S_3, IT, SI and SIT; (b) Tauc plots of TiO_2, In_2S_3 and Sb_2S_3; (c) X-ray photoemission valence spectra of TiO_2, In_2S_3 and Sb_2S_3; (d) UPS profiles of TiO_2, In_2S_3 and Sb_2S_3.

Fig. 6(a). IT similar to In_2S_3 shows a photo-absorption edge at 577 nm, which was also improved due to the presence of TiO_2. SI is similar to Sb_2S_3 and shows a light absorption edge at 709 nm. In addition, after modifying Sb_2S_3 on IT. The photo-absorption of SIT has been broadened (edge: 654 nm) compared with that of IT. The optical band gap was calculated using linear extrapolation of the Tauc plot based on the Kubelka–Munk function (eqn (S1)†), as shown in Fig. 10(b).[25] The band gap values for TiO_2, In_2S_3, and Sb_2S_3 were estimated to be about 2.93, 2.19, and 1.86 eV.

According to the results of XPS valence band (VB) spectra (Fig. 10(c)), the VB of TiO_2, In_2S_3, and Sb_2S_3 are 2.35 eV, 1.14 eV, and 0.48 eV, respectively. The UPS spectra with cutoff energy (E_{cutoff}) at high binding energy are shown in Fig. 10(c). When Fermi levels (E_F) are consistent with 0 eV, the corresponding E_{cutoff} of TiO_2, In_2S_3 and Sb_2S_3 are 15.47 eV, 15.74 eV and 15.49 eV, respectively.[36] Therefore, as calculated by eqn (S4),† the work functions of TiO_2, In_2S_3, and Sb_2S_3 are 2.35 eV, 1.14 eV, and 0.48 eV, respectively.

Because of the contact potential difference between the sample and the XPS analyzer, the VB location of the sample with respect to the general hydrogen electrode (NHE) can be estimated using the formula in eqn (1):[36]

$$E_{VB} = E_{VB\text{–}XPS} + \varphi - 4.44 \quad (1)$$

where E_{VB} is the VB potential relative to NHE, $E_{VB\text{-}XPS}$ is the observed value of the VB-XPS and φ is the electron work function of the XPS analyzer (4.55 eV). Following thorough computations, the E_{VB} of TiO_2, In_2S_3 and Sb_2S_3 are, respectively, +2.75 V *vs.* NHE, +1.25 V *vs.* NHE, and +0.59 V *vs.* NHE. The location of the conduction band (CB) of photocatalyst can be calculated by the following eqn (2):[22]

$$E_{CB} = E_g - E_{VB} \quad (2)$$

where E_{CB} is the CB potential relative to NHE. The CB of TiO_2, Sb_2S_3 and In_2S_3 are −0.18 V *vs.* NHE, −0.94 V *vs.* NHE and −1.27 V *vs.* NHE, respectively. As shown in Fig. 11(a), the bands of the three photocatalysts show cross-alignment. Therefore, a distinctive charge transfer pathway for the SIT system that is consistent with the dual Z-type heterojunction mechanism is presented in this study based on the appropriate conduction band potentials and valence band potentials of the photocatalysts.[19]

Two potential charge transfer modes type II heterojunction and Z-type heterojunction – are suggested for SIT photocatalytic degradation of LEV based on the results from the previous analysis (Fig. 11).[33] Together with Fig. 11(c), photogenerated holes will go from the VB of TiO_2 to the VB of In_2S_3 and Sb_2S_3, whereas photogenerated electrons will move from the CB of In_2S_3 and Sb_2S_3 to the CB of TiO_2. The electrons in the CB of TiO_2 are unable to decrease $O_2/{}^{\bullet}O_2^-$ because the CB potential of

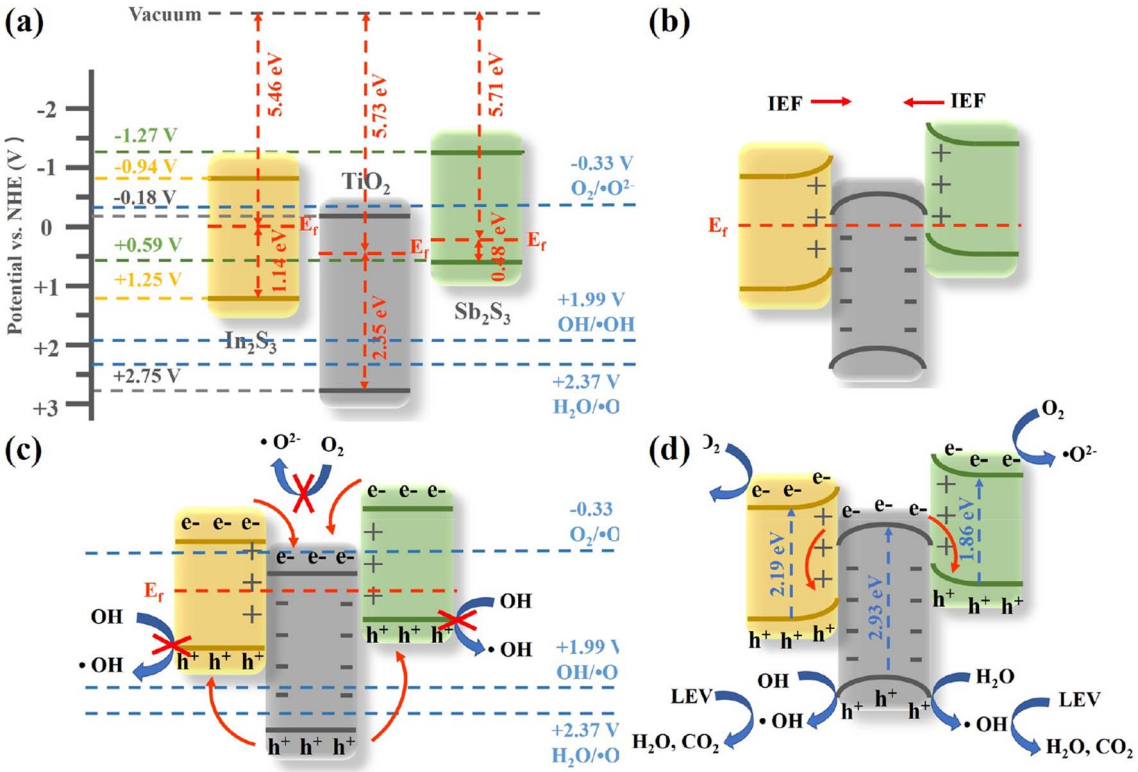

Fig. 11 (a) Band structure diagram of TiO_2, In_2S_3 and Sb_2S_3; (b–d) schematic illustration of charge transfer mechanism occurring through traditional type-II pathway and direct Z-type pathway in SIT system under visible light irradiation.

TiO_2 (−0.18 V *vs.* NHE) is more positive than the typical superoxide radical potential $O_2/{}^{\bullet}O_2^-$ (−0.33 V *vs.* NHE).[17] Additionally, the In_2S_3 and Sb_2S_3 cavities in VB do not have enough oxidation capacity to make ${}^{\bullet}OH$ since the VB of In_2S_3 and Sb_2S_3 (+1.25 and +0.59 V *vs.* NHE, respectively) is more negative than the usual redox potentials $H_2O/{}^{\bullet}OH$ (+2.37 V *vs.* NHE) and $OH^-/{}^{\bullet}OH$ (+1.99 V *vs.* NHE).[18] If the SIT interface is a conventional type II heterojunction, then there should be no signal for ${}^{\bullet}OH$ and ${}^{\bullet}O_2^-$. However, signals for ${}^{\bullet}OH$, ${}^{\bullet}O_2^-$ and h^+ were observed in radical trapping experiments and EPR spectroscopy; therefore, the charge transfer in SIT is not a type II heterojunction.

The reaction mechanism for the degradation of LEV by the SIT dual Z-type heterojunction suggested in this research is shown in Fig. 11(d) based on the data mentioned above. As shown in Fig. 11(a), the Fermi energy levels (E_F) of In_2S_3 and Sb_2S_3 are higher than those of TiO_2 prior to contact. When $Sb_2S_3/In_2S_3/TiO_2$ are successfully compounded, a heterojunction is formed between them and electrons migrate from the In_2S_3 and Sb_2S_3 interfaces to TiO_2 until the E_F of the three semiconductors reach equilibrium. The electron transfer paths are consistent with those determined using high-resolution XPS. At the same time, an internal electric field (IEF) was formed in the interface region and pointed from In_2S_3 and Sb_2S_3 to TiO_2. Thereafter, photogenerated electrons migrated from TiO_2 to In_2S_3 and Sb_2S_3 under light irradiation driven by the IEF (Fig. 11(b)). Notably, IEF was present, which supported the results of photoelectrochemical tests by facilitating electron transfer and strongly hindered the complexation of photogenerated carriers.[23] Furthermore, the IEF increased the electronic potential energy of In_2S_3 and Sb_2S_3 and decreased that of TiO_2, resulting in the energy band edges of In_2S_3 and Sb_2S_3 showing an upward band bend and that of TiO_2 showing a downward band bend (Fig. 11(b)). Energy band variations are a prominent feature of Z-scheme heterojunctions, a charge transport pathway that greatly increases separation rates and reduces recombination of photogenerated electron–hole pairs.

Electrons in TiO_2, In_2S_3, and Sb_2S_3 are stimulated by photons when exposed to visible light (eqn (3)–(5)).[25] With the help of IEF, electrons in the CB of TiO_2 bind to holes in the VB of In_2S_3 and Sb_2S_3 (eqn (6) and (7)),[45] isolating the holes of TiO_2 and the electrons of In_2S_3 and Sb_2S_3 to the greatest extent possible. Additionally, the superoxide radical potential of $O_2/{}^{\bullet}O_2^-$ is less negative than the CB energy levels of In_2S_3 and Sb_2S_3, allowing the electrons in In_2S_3 and Sb_2S_3 with high reducing capacity to convert adsorbed O_2 to ${}^{\bullet}O_2^-$ (eqn (8) and (9)).[22] After that, some of the ${}^{\bullet}O_2^-$ reacts with the H^+ to create H_2O_2 (eqn (10) and (11)).[19] H_2O_2 then undergoes a second reaction with ${}^{\bullet}O_2^-$ to produce OH (eqn (12)).[36] The strongly oxidizing h^+ in TiO_2 can oxidize H_2O and OH^- to generate ${}^{\bullet}OH$ since the VB level of TiO_2 is higher than the usual redox potentials of $H_2O/{}^{\bullet}OH$ and $OH^-/{}^{\bullet}OH$. Also, the holes left on TiO_2 can directly capture the electrons in LEV molecules and oxidize them directly. Therefore, the degradation of LEVs in SIT systems is dominated by radicals such as ${}^{\bullet}OH$, ${}^{\bullet}O_2^-$ and h^+ (eqn (15)).[24] As a result, the charge transfer in SIT is a Z-type heterojunction, and the successful

construction of the Z-type heterojunction enables the efficient separation and transfer of photogenerated electrons and holes of the three semiconductors, while the strongly oxidizing holes are retained in the CB of TiO_2 and the strongly reducing electrons are retained in the VB of In_2S_3 and Sb_2S_3. As a result, the SIT system successfully degrades LEV by photocatalysis. The possible reaction steps are shown in eq:

$$TiO_2 + h\nu = TiO_2\ (e^- + h^+) \quad (3)$$

$$In_2S_3 + h\nu = In_2S_3\ (e^- + h^+) \quad (4)$$

$$Sb_2S_3 + h\nu = Sb_2S_3\ (e^- + h^+) \quad (5)$$

$$TiO_2\ (e^-) + In_2S_3\ (h^+) \rightarrow TiO_2 + In_2S_3 \quad (6)$$

$$TiO_2\ (e^-) + Sb_2S_3\ (h^+) \rightarrow TiO_2 + Sb_2S_3 \quad (7)$$

$$In_2S_3\ (e^-) + (O_2)_{abs} \rightarrow In_2S_3 + {}^{\bullet}O_2^- \quad (8)$$

$$Sb_2S_3\ (e^-) + (O_2)_{abs} \rightarrow Sb_2S_3 + {}^{\bullet}O_2^- \quad (9)$$

$${}^{\bullet}O_2^- + H^+ = {}^{\bullet}OOH \quad (10)$$

$$H_2O_2 + {}^{\bullet}O_2^- = {}^{\bullet}OH + OH^- + O_2 \quad (11)$$

$${}^{\bullet}OOH + {}^{\bullet}OOH = H_2O_2 \quad (12)$$

$$TiO_2\ (h^+) + H_2O \rightarrow TiO_2 + {}^{\bullet}OH + H^+ \quad (13)$$

$$TiO_2\ (h^+) + OH^- \rightarrow TiO_2 + {}^{\bullet}OH \quad (14)$$

$${}^{\bullet}OH/{}^{\bullet}O_2^-/h^+ + LEV = CO_2 + HO_2 + \text{small molecules} \quad (15)$$

4. Conclusion

In this study, Z-type $Sb_2S_3/In_2S_3/TiO_2$ (SIT) heterojunction photocatalysts were constructed by anchoring In_2S_3 nanosheets and Sb_2S_3 nanoparticles to form a layered structure on TiO_2 nanorod arrays using a simple two-step hydrothermal method. The morphology and structure of the SIT photocatalysts were accurately described using XRD, SEM, TEM and XPS. Under visible light, the Z-type SIT catalyst exhibited excellent photocatalytic activity in the degradation of levofloxacin (LEV) with a high degradation efficiency of 86.7%. The kinetic rate was 1.44×10^{-2} min^{-1}, which was 2.36 and 1.25 times higher than that of TiO_2 and In_2S_3/TiO_2 (IT) composites, respectively. Under the same experimental conditions, the SIT photocatalytic system also exhibited excellent photocatalytic degradation activities for CHI, GAT and AMP, with degradation efficiencies of 81.2%, 67.0% and 28.8%, respectively, which indicated that the material has a wide range of applicability to antibiotics. Meanwhile, the main oxidising radicals in the photocatalytic system were identified as ${}^{\bullet}O_2^-$ and ${}^{\bullet}OH$ by capture experiments and electron spin resonance spectroscopy (EPR), and the degradation pathways and intermediates of LEVs were revealed by liquid chromatography mass spectrometry (LC-MS) and three-dimensional excitation–emission matrix fluorescence (3D EEMs). In addition, PL, TRPL, UV-visible and photoelectrochemical property tests were carried out, which demonstrated the excellent full-spectrum responsiveness and charge separation and transfer ability of SIT, formulated the energy band structure of the Z-type heterojunction, and proposed the degradation steps and mechanism of the Z-type SIT photocatalyst. Overall, this study provides novel insights into the degradation of antibiotics using thin-film photocatalysts.

Author contributions

Jianrou Li: investigation, writing-original draft. Zhuangzhuang Yin: investigation, formal analysis. Jun Guo: visualization, formal analysis. Wei Gan: visualization, software. Ruixin Chen: investigation, visualization. Miao Zhang: formal analysis. Zhaoqi Sun: funding acquisition.

Conflicts of interest

There are no conflicts to declare.

Acknowledgements

This study is supported by the National Natural Science Foundation of China (No. 51772003, 51472003 and 51701001). The authors are also grateful to Huimin Fang, Jun Zheng, Zhongqing Lin, Xiuzhen Zhang and Shenqiang Zhao of the Experimental Technology Center for providing support with the microstructure characterization. The authors also like to thank Lei He from Shiyanjia Lab (**https://www.shiyanjia.com**) for the Electron Paramagnetic Resonance (EPR) analysis.

Notes and references

1 L. He, S. Yang, S. Shen, Y. Ma, Y. Chen, J. Xue, J. Wang, L. Zheng, L. Wu, Z. Zhang and L. Yang, Novel insights into the mechanism of periodate activation by heterogeneous ultrasonic-enhanced sludge biochar: Relevance for efficient degradation of levofloxacin, *J. Hazard. Mater.*, 2022, **434**, 128860.

2 Q. Y. Jin, D. Y. Ji, Y. H. Chen, Z. M. Tang and Y. S. Fu, Kinetics and pathway of levofloxacin degradation by ferrate(VI) and reaction mechanism of catalytic degradation by copper sulfide, *Sep. Purif. Technol.*, 2022, **282**, 120104.

3 J. Cai, Y. Zhang, T. Qian, X. Li, Z. Chen and L. Zhang, Bismuth oxybromide/bismuth oxyiodide nanojunctions decorated on flexible carbon fiber cloth as easily recyclable photocatalyst for removing various pollutants from wastewater, *J. Colloid Interface Sci.*, 2022, **608**, 2660–2671.

4 Q. C. Deng, X. D. Zhang, L. Chang, H. X. Chai and Y. M. Huang, The MOF/LDH derived heterostructured $Co_3O_4/MnCo_2O_4$ composite for enhanced degradation of levofloxacin by peroxymonosulfate activation, *Sep. Purif. Technol.*, 2022, **294**, 121182.

5 Y. Zhao, H. Guo, J. Liu, Q. Xia, J. Liu, X. Liang, E. Liu and J. Fan, Effective photodegradation of rhodamine B and

levofloxacin over CQDs modified BiOCl and BiOBr composite: Mechanism and toxicity assessment, *J. Colloid Interface Sci.*, 2022, **627**, 180–193.

6 Z. Fang, Z. Zhou, G. Xue, Y. Yu, Q. Wang, B. Cheng, Y. Ge and Y. Qian, Application of sludge biochar combined with peroxydisulfate to degrade fluoroquinolones: Efficiency, mechanisms and implication for ISCO, *J. Hazard. Mater.*, 2022, **426**, 128081.

7 C. K. Tsai, Y. C. Lee, T. T. Nguyen and J. J. Horng, Levofloxacin degradation under visible-LED photocatalyzing by a novel ternary Fe-ZnO/WO_3 nanocomposite, *Chemosphere*, 2022, **298**, 134285.

8 J. K. Nie, X. J. Yu, Z. B. Liu, Y. C. Wei, J. Zhang, N. N. Zhao, Z. Yu and B. H. Yao, Boosting principles for the photocatalytic performance of Cr-doped CuO crystallites and mechanisms of photocatalytic oxidation for levofloxacin, *Appl. Surf. Sci.*, 2022, **576**, 151842.

9 T. Qian, Y. Zhang, J. Cai, W. Cao, T. Liu, Z. Chen, J. Liu, F. Li and L. Zhang, Decoration of amine functionalized zirconium metal organic framework/silver iodide heterojunction on carbon fiber cloth as a filter- membrane-shaped photocatalyst for degrading antibiotics, *J. Colloid Interface Sci.*, 2021, **603**, 582–593.

10 Z. R. Deng, X. Y. Zheng and Y. F. Guo, Effective degradation of doxycycline hydrochloride in simulated and real water by S-scheme heterojunction 2D/1D $Bi_4O_5I_2/In_2O_3$ under visible light: DFT calculation, mechanism, degradation pathway and toxicity analysis, *Appl. Surf. Sci.*, 2023, **641**, 158407.

11 Z. Deng, Y. Li, X. Zheng and Y. Guo, Photocatalytic activity evaluation of polyvinylpyrrolidone K30 assisted synthesis of 1D oxygen-vacancy-rich $Bi_5O_7Br_xI_{1-x}$ nanorod solid solution, *J. Hazard. Mater.*, 2024, **465**, 133361.

12 J. J. Cheng, Z. R. Deng, X. Y. Zheng, C. Y. Chu and Y. F. Guo, Construction and actual application of In_2O_3/BiOBr heterojunction for effective removal of ciprofloxacin under visible light: Photocatalytic mechanism, DFT calculation,degradation pathway and toxicity evaluation, *J. Alloys Compd.*, 2024, **971**, 172779.

13 Z. Zeng, Z. R. Deng, T. Wang, H. S. Huang and Y. F. Guo, Environmentally friendly synthesis of S-scheme heterojunction UiO-66-NH_2/$Bi_7O_9I_3$ for promoted degradation of ciprofloxacin under visible light: DFT calculation, degradation mechanism and toxicity evaluation, *Sep. Purif. Technol.*, 2023, **311**, 123264.

14 Y. Liang, G. Huang, X. Xin, Y. Yao, Y. Li, J. Yin, X. Li, Y. Wu and S. Gao, Black titanium dioxide nanomaterials for photocatalytic removal of pollutants: A review, *J. Mater. Sci. Technol.*, 2022, **112**, 239–262.

15 L. Wang, X. Fei, L. Zhang, J. Yu, B. Cheng and Y. Ma, Solar fuel generation over nature-inspired recyclable TiO_2/g-C_3N_4 S-scheme hierarchical thin-film photocatalyst, *J. Mater. Sci. Technol.*, 2022, **112**, 1–10.

16 S. Zhang, S. Sun, B. Huang, N. Wang and X. Li, UV-Enhanced Formaldehyde Sensor Using Hollow In_2O_3@TiO_2 Double-Layer Nanospheres at Room Temperature, *ACS Appl. Mater. Interfaces*, 2023, **15**, 4329–4342.

17 C. Hu, L. Chen, Y. Hu, A. Chen, L. Chen, H. Jiang and C. Li, Light-Motivated SnO_2/TiO_2 Heterojunctions Enabling the Breakthrough in Energy Density for Lithium-Ion Batteries, *Adv. Mater.*, 2021, **33**, 2103558.

18 L. Wang, B. Cheng, L. Zhang and J. Yu, In situ Irradiated XPS Investigation on S-Scheme TiO_2@$ZnIn_2S_4$ Photocatalyst for Efficient Photocatalytic CO_2 Reduction, *Small*, 2021, **17**, 2103447.

19 W. Gan, X. C. Fu, J. Guo, M. Zhang, H. Yu, C. S. Ding, S. A. Qi, X. Y. Cao and Z. Q. Sun, Facile synthesis of mesoporous hierarchical TiO_2 micro-flowers serving as the scaffolding of 0D Ag_3PO_4 nanoparticles for the ultra-fast degradation of organic pollutants, *J. Alloys Compd.*, 2022, **909**, 164737.

20 Z. T. Dong, C. G. Niu, H. Guo, H. Y. Niu, S. Liang, C. Liang, H. Y. Liu and Y. Y. Yang, Anchoring $CuFe_2O_4$ nanoparticles into N-doped carbon nanosheets for peroxymonosulfate activation: Built-in electric field dominated radical and non-radical process, *Chem. Eng. J.*, 2021, **426**, 130850.

21 Z. Pang, P. Luo, C. Wei, Z. Qin, T. Wei, Y. Hu, H. Wu and C. Wei, In-situ growth of Co/Ni bimetallic organic frameworks on carbon spheres with catalytic ozonation performance for removal of bio-treated coking wastewater, *Chemosphere*, 2022, **291**, 132874.

22 W. Gan, X. Fu, J. Jin, J. Guo, M. Zhang, R. Chen, C. Ding, Y. Lu, J. Li and Z. Sun, Nitrogen-rich carbon nitride (C_3N_5) coupled with oxygen vacancy TiO2 arrays for efficient photocatalytic H2O2 production, *J. Colloid Interface Sci.*, 2024, **653**, 1028–1039.

23 Y. Tao, Z. Ma, W. C. Wang, C. Zhang, L. L. Fu, Q. Zhu, Y. L. Li, G. S. Li and D. Q. Zhang, Nickel Phosphide Clusters Sensitized TiO_2 Nanotube Arrays as Highly Efficient Photoanode for Photoelectrocatalytic Urea Oxidation, *Adv. Funct. Mater.*, 2023, **33**, 2211169.

24 W. Gan, X. C. Fu, J. Guo, M. Zhang, D. D. Li, C. S. Ding, Y. Q. Lu, P. Wang and Z. Q. Sun, Ag nanoparticles decorated 2D/2D TiO_2/g-C_3N_4 heterojunction for efficient removal of tetracycline hydrochloride: Synthesis, degradation pathways, and mechanism, *Appl. Surf. Sci.*, 2022, **606**, 154837.

25 J. Guo, W. Gan, C. S. Ding, Y. Q. Lu, J. R. Li, S. H. Qi, M. Zhang and Z. Q. Sun, Black phosphorus quantum dots and Ag nanoparticles co-modified TiO_2 nanorod arrays as powerful photocatalyst for tetracycline hydrochloride degradation: Pathways, toxicity assessment, and mechanism insight, *Sep. Purif. Technol.*, 2022, **297**, 1383–5866.

26 J. Jiang, X. Wang, C. Yue, S. Liu, Y. Lin, T. Xie and S. Dong, Efficient photoactivation of peroxymonosulfate by Z-scheme nitrogen-defect-rich $NiCo_2O_4$/g-C_3N_4 for rapid emerging pollutants degradation, *J. Hazard. Mater.*, 2021, **414**, 125528.

27 F. Z. Chen, Y. J. Li, M. Zhou, X. X. Gong, Y. Gao, G. Cheng, S. B. Ren and D. M. Han, Smart multifunctional direct Z-scheme In_2S_3@PCN-224 heterojunction for simultaneous detection and photodegradation towards antibiotic pollutants, *Appl. Catal., B*, 2023, **328**, 122517.

28 B. Geng, S. Zhang, X. Yang, W. Shi, P. Li, D. Pan and L. Shen, $Cu_{2-x}O@TiO_{2-y}$ Z-type heterojunctions for sonodynamic-chemodynamic combined tumor eradication, *Chem. Eng. J.*, 2022, **435**, 134777.

29 X. Zheng, T. Liu, J. Wen and X. Liu, Flower-like Bi_2S_3-In_2S_3 heterojunction for efficient solar light induced photoreduction of Cr(VI), *Chemosphere*, 2021, **278**, 130422.

30 J. Park, T. H. Lee, C. Kim, S. A. Lee, M. J. Choi, H. Kim, J. W. Yang, J. Lim and H. W. Jang, Hydrothermally obtained type-II heterojunction nanostructures of In_2S_3/TiO_2 for remarkably enhanced photoelectrochemical water splitting, *Appl. Catal., B*, 2021, **295**, 120276.

31 C. Z. Zhu, H. Q. Yao, S. K. Le, Y. Yin, C. X. Chen, H. T. Xu, S. B. Wang and X. G. Duan, S-scheme photocatalysis induced by ultrathin TiO_2(B) nanosheets-anchored hierarchical In_2S_3 spheres for boosted photocatalytic activity, *Composites, Part B*, 2022, **242**, 110082.

32 Y. Xiao, H. Wang, Y. Jiang, W. Zhang, J. Zhang, X. Wu, Z. Liu and W. Deng, Hierarchical Sb_2S_3/$ZnIn_2S_4$ core-shell heterostructure for highly efficient photocatalytic hydrogen production and pollutant degradation, *J. Colloid Interface Sci.*, 2022, **623**, 109–123.

33 Z. Y. Zhu, J. Y. Li, W. Li, X. Y. Liu, Y. Y. Dang, T. H. Ma and C. Y. Wang, Simulated-sunlight-driven Cr(VI) reduction on a type-II heterostructured Sb_2S_3/CdS photocatalyst, *Environ. Sci.: Nano*, 2022, **9**, 1738–1747.

34 J. Zhao, Y. Cheng, Y. Chen, W. Zhang, E. Liu, J. Fan, H. Miao and X. Hu, Defects regulation of Sb_2S_3 by construction of Sb_2S_3/In_2S_3 direct Z-type heterojunction with enhanced photoelectrochemical performance, *Appl. Surf. Sci.*, 2021, **568**, 150917.

35 K. W. Wang, Z. P. Huang and J. Wang, Synthesis of hierarchical tandem double Z-scheme heterojunctions for robust photocatalytic H_2 generation, *Chem. Eng. J.*, 2022, **430**, 132727.

36 C. S. Ding, Y. Q. Lu, J. Guo, W. Gan, S. H. Qi, Z. Z. Yin, M. Zhang and Z. Q. Sun, Internal electric field-mediated sulfur vacancies-modified-In_2S_3/TiO_2 thin-film heterojunctions as a photocatalyst for peroxymonosulfate activation: Density functional theory calculations, levofloxacin hydrochloride degradation pathways and toxicity of intermediates, *Chem. Eng. J.*, 2022, **450**, 138271.

37 S. Sharma and S. Basu, Fabrication of centimeter-sized Sb_2S_3/SiO_2 monolithic mimosa pudica nanoflowers for remediation of hazardous pollutants from industrial wastewater, *J. Cleaner Prod.*, 2021, **280**, 124525.

38 M. L. Tang, Y. H. Ao, C. Wang and P. F. Wang, Rationally constructing of a novel dual Z-scheme composite photocatalyst with significantly enhanced performance for neonicotinoid degradation under visible light irradiation, *Appl. Catal., B*, 2020, **270**, 118918.

39 T. Garg, Renu, J. Kaur, P. Kaur, Nitansh, V. Kumar, K. Tikoo, A. Kaushik and S. Singhal, An innovative Z-type g-C_3N_4/ZnO/$NiFe_2O_4$ heterostructure for the concomitant photocatalytic removal and real-time monitoring of noxious fluoroquinolones, *Chem. Eng. J.*, 2022, **443**, 136441.

40 X. Chen, R. T. Guo, W. G. Pan, Y. Yuan, X. Hu, Z. X. Bi and J. Wang, A novel double S-scheme photocatalyst $Bi_7O_9I_3$/$Cd_{0.5}Zn_{0.5}S$ QDs/WO_{3-x} with efficient full-spectrum-induced phenol photodegradation, *Appl. Catal., B*, 2022, **318**, 121839.

41 H. Sepehrmansourie, H. Alamgholiloo, N. N. Pesyan and M. A. Zolfigol, A MOF-on-MOF strategy to construct double Z-scheme heterojunction for high-performance photocatalytic degradation, *Appl. Catal., B*, 2023, **321**, 122082.

42 M. L. Ren, Y. H. Ao, P. F. Wang and C. Wang, Construction of silver/graphitic-C_3N_4/bismuth tantalate Z-scheme photocatalyst with enhanced visible-light-driven performance for sulfamethoxazole degradation, *Chem. Eng. J.*, 2019, **378**, 122122.

43 Y. Guo, Y. H. Ao, P. F. Wang and C. Wang, Mediator-free direct dual-Z-scheme Bi_2S_3/$BiVO_4$/$MgIn_2S_4$ composite photocatalysts with enhanced visible-light-driven performance towards carbamazepine degradation, *Appl. Catal., B*, 2019, **254**, 479–490.

44 S. S. M. Bhat, S. A. Pawar, D. Potphode, C.-K. Moon, J. M. Suh, C. Kim, S. Choi, D. S. Patil, J.-J. Kim, J. C. Shin and H. W. Jang, Substantially enhanced photoelectrochemical performance of TiO_2 nanorods/CdS nanocrystals heterojunction photoanode decorated with MoS_2 nanosheets, *Appl. Catal., B*, 2019, **259**, 118102.

45 S. A. Qi, Z. Z. Yin, Z. Liu, K. Xu, M. Zhang and Z. Q. Sun, Construction of In_2S_3/Ag-Ag_2S-$AgInS_2$/TNR Nanoarrays with Excellent Photoelectrochemical and Photocatalytic Properties, *J. Electrochem. Soc.*, 2021, **168**, 126517.

46 Y. Chen, Y. Cheng, J. Zhao, W. Zhang, J. Gao, H. Miao and X. Hu, Construction of Sb_2S_3/CdS/$CdIn_2S_4$ cascaded S-scheme heterojunction for improving photoelectrochemical performance, *J. Colloid Interface Sci.*, 2022, **627**, 1047–1060.

47 J. Shen, L. Qian, J. Huang, Y. Guo and Z. Zhang, Enhanced degradation toward Levofloxacin under visible light with S-scheme heterojunction In_2O_3/Ag_2CO_3: Internal electric field, DFT calculation and degradation mechanism, *Sep. Purif. Technol.*, 2021, **275**, 119239.

48 J. M. Li, C. C. Wu, J. Li, B. H. Dong, L. Zhao and S. M. Wang, 1D/2D TiO_2/$ZnIn_2S_4$ S-scheme heterojunction photocatalyst for efficient hydrogen evolution, *Chin. J. Catal.*, 2022, **43**, 339–349.

49 L. Chen, X. L. Song, J. T. Ren and Z. Y. Yuan, Precisely modifying Co_2P/black TiO_2 S-scheme heterojunction by in situ formed P and C dopants for enhanced photocatalytic H_2 production, *Appl. Catal., B*, 2022, **315**, 121546.

50 J. Shen, L. Qian, J. Huang, Y. Guo and Z. Zhang, Enhanced degradation toward Levofloxacin under visible light with S-scheme heterojunction In_2O_3/Ag_2CO_3: Internal electric field, DFT calculation and degradation mechanism, *Sep. Purif. Technol.*, 2021, **275**, 119239.

51 M. H. Elbakkay, W. M. A. El Rouby, A. Mariño-López, A. Sousa-Castillo, V. Salgueiriño, S. I. El-Dek, A. A. Farghali, M. A. Correa-Duarte and P. Millet, One-pot synthesis of TiO_2/Sb_2S_3/RGO complex multicomponent heterostructures for highly enhanced photoelectrochemical water splitting, *Int. J. Hydrogen Energy*, 2021, **46**, 31216–31227.